RESEARCH

A Dual-Species Atom Interferometer Payload for Operation on Sounding Rockets

Michael Elsen[1] · Baptist Piest[2] · Fabian Adam[3] · Oliver Anton[4] · Paweł Arciszewski[4] · Wolfgang Bartosch[2] · Dennis Becker[2] · Kai Bleeke[5] · Jonas Böhm[2] · Sören Boles[6] · Klaus Döringshoff[4] · Priyanka Guggilam[2] · Ortwin Hellmig[11] · Isabell Imwalle[2] · Simon Kanthak[4] · Christian Kürbis[10] · Matthias Koch[2] · Maike Diana Lachmann[2] · Moritz Mihm[6] · Hauke Müntinga[3] · Ayush Mani Nepal[5] · Tim Oberschulte[7] · Peter Ohr[5] · Alexandros Papakonstantinou[2] · Arnau Prat[5] · Christian Reichelt[2] · Jan Sommer[5] · Christian Spindeldreier[7] · Marvin Warner[1] · Thijs Wendrich[2] · André Wenzlawski[6] · Holger Blume[7] · Claus Braxmaier[8,9] · Daniel Lüdtke[5] · Achim Peters[4] · Ernst Maria Rasel[2] · Klaus Sengstock[11] · Andreas Wicht[10] · Patrick Windpassinger[6] · Jens Grosse[1]

Abstract
We report on the design and the construction of a sounding rocket payload capable of performing atom interferometry with Bose-Einstein condensates of ^{41}K and ^{87}Rb. The apparatus is designed to be launched in two consecutive missions with a VSB-30 sounding rocket and is qualified to withstand the expected vibrational loads of 1.8 g root-mean-square in a frequency range between 20–2000 Hz and the expected static loads during ascent and re-entry of 25 g. We present a modular design of the scientific payload comprising a physics package, a laser system, an electronics system and a battery module. A dedicated on-board software provides a largely automated process of predefined experiments. To operate the payload safely in laboratory and flight mode, a thermal control system and ground support equipment has been implemented and will be presented. The payload presented here represents a cornerstone for future applications of matter wave interferometry with ultracold atoms on satellites.

Keywords Bose-Einstein condensate · Quantum optics · Atom optics · Atom interferometry · Microgravity · Sounding rocket

✉ Michael Elsen
michael.elsen@zarm.uni-bremen.de

1. Zentrum für angewandte Raumfahrttechnologie und Mikrogravitation, Universität Bremen, Am Fallturm, 28359 Bremen, Germany

2. Institut für Quantenoptik, Leibniz Universität Hannover, Welfengarten 1, 30167 Hannover, Germany

3. Institut für Satellitengeodäsie und Inertialsensorik, Deutsches Zentrum für Luft und Raumfahrt e.V., Callinstr. 30b, 30167 Hannover, Germany

4. Institut für Physik, Humboldt-Universität zu Berlin, Newtonstraße 15, 12489 Berlin, Germany

5. Institut für Softwaretechnologie, Deutsches Zentrum für Luft und Raumfahrt e.V., Lilienthalplatz 7, 38108 Braunschweig, Germany

6. Institut für Physik, Johannes Gutenberg-Universität Mainz, 55099 Mainz, Germany

7. Institut für Mikroelektronische Systeme, Leibniz Universität Hannover, Appelstraße 4, 30167 Hannover, Germany

8. Institut für Mikroelektronik, Universität Ulm, Albert-Einstein-Allee 43, 89081 Ulm, Germany

9. Institut für Quantentechnologie, Deutsches Zentrum für Luft und Raumfahrt e.V., Wilhelm-Runge-Str. 10, 89081 Ulm, Germany

10. Ferdinand-Braun-Institut, Leibniz-Institut für Höchstfrequenztechnik, Gustav-Kirchhoff-Str. 4, 12489 Berlin, Germany

11. Institute of Laser-Physics, University Hamburg, Luruper Chaussee 149, 22761 Hamburg, Germany

Introduction

Space offers great potential for studies of fundamental physics with cold atoms, such as tests of the universality of free fall (Aguilera et al. 2014; Ahlers et al. 2022) and the detection of gravitational waves (Loriani et al. 2019). Utilizing free-falling atoms of two different species as sensitive probes for differential inertial forces, light-pulse atom interferometry enables to test the Einstein equivalence principle (EEP) with high accuracy (Schlippert et al. 2014; Zhou et al. 2015; Asenbaum et al. 2020). For such atom interferometers the sensitivity for measuring inertial forces acting on the atomic cloud scales quadratically with the free fall time. One way to extend current limitations on the free fall time, typically set by the size of the baseline, is to perform measurements on microgravity platforms such as drop towers, parabola flights, sounding rockets or satellites instead of ground based setups. Working with long free fall times, however, requires the production of Bose-Einstein condensates (BECs) due to their small initial size and narrow momentum distribution. The complexity of such experiments and high demands regarding stability and accuracy face us with enormous challenges when transferring the sensitive setups into space.

Recent missions on sub-orbital and orbital platforms show a fast progress towards high precision measurements with atom optical instruments (Gaaloul et al. 2022; Carollo et al. 2022; Becker et al. 2018; Liu et al. 2018; Condon et al. 2019) in microgravity environments. Sounding rockets offer excellent microgravity conditions and a comparably easy accessible and economically affordable platform. In the beginning of 2017, the sounding rocket mission MAIUS-1 (**Ma**teriewellen**i**nterferometrie **u**nter **S**chwerelosigkeit, matter wave interferometry in microgravity) successfully demonstrated the first BEC of ^{87}Rb in space and conducted further experiments studying their coherence properties using atom interferometry (Becker et al. 2018; Lachmann et al. 2021).

To go one step further, two additional sounding rocket missions MAIUS-2/3 are planned with a newly developed payload to measure the differential accelerations of two BECs consisting of different species, ^{87}Rb and ^{41}K. With these measurements, the experiments pave the way for tests of the equivalence principle in space with unprecedented sensitivity. The technologies developed for these missions show a pathway towards future endeavours on space based platforms with ultracold atoms (Alonso et al. 2022) like the international space station (ISS) (Frye et al. 2019) or satellite missions such as CARIOQA (Lévèque et al. 2022) or STE-QUEST (Aguilera et al. 2014; Ahlers et al. 2022).

The generation of dual species BEC mixtures on a sounding rocket requires the development of a new apparatus with extended capabilities compared to the single species system of MAIUS-1 (Grosse 2016; Schkolnik et al. 2016). This paper gives a detailed overview of the payload of MAIUS-2/3, named MAIUS-B, with a focus on its technical implementation and qualification and is organized as follows: "Experimental Methods" section gives a brief overview of the mission objectives and the experimental capabilities of the apparatus. "Description of Apparatus" section will provide a description of the scientific payload which consists of different modules containing the experimental chamber, laser system and electronics system. Also, a discussion of the thermal control system (TCS) and the structure of the software is provided. In "Qualification Process", section the qualification process is described and results of vibrational tests are presented.

Experimental Methods

The goal of the MAIUS-2/3 missions is to measure the differential accelerations of two free falling ultracold atom clouds of different atomic species revealing an EEP test. Due to their difference in mass and their magnetically tunable interatomic interactions ^{87}Rb and ^{41}K are appropriate candidates for such studies (Thalhammer et al. 2008). Furthermore they offer optical transitions capable of laser cooling in a similar frequency range which simplifies the setup of the laser system. Their preparation in high atom number, low expansion velocity and large overlap is crucial for the signal and the suppression of systematic effects. The new apparatus MAIUS-B is able to autonomously create single- or dual-species BECs containing ^{87}Rb and ^{41}K with state-of-the-art repetition rates and particle numbers using an integrated atom chip. The chip is suitable for magnetic delta-kick collimation techniques (Ammann and Christensen 1997; Deppner et al. 2021; Corgier et al. 2020) of both species to lower their expansion velocity enabling a long pulse-separation time in the atom interferometer. It further allows for fast transport of the atomic ensembles to the desired interferometer region within the science chamber (Corgier et al. 2018). Employing optical gratings based on Raman double-diffraction (Leveque et al. 2009; Hartmann et al. 2020) the apparatus can perform atom interferometry with the free falling BECs. The rotation rate control system of the sounding rocket allows to conduct atom interferometric measurements up to $T = 50$ ms without any significant loss of contrast or additional Sagnac phase shifts due to the rotation of the system (Roura et al. 2014; Berg et al. 2015).

A typical experimental sequence to prepare these mixtures starts with loading of a three-dimensional chip magneto-optical trap (MOT, Wildermuth et al. (2004)) with ^{87}Rb and ^{41}K atoms from a cold atomic beam. Afterwards, the atoms are further cooled to sub-Doppler temperatures in a molasses stage and optically pumped into the low-field seeking states

$|F = 2, m_F = 2\rangle$ in order to load them into a cigar shaped harmonic magnetic trap, provided by the atom chip with trapping frequencies of $\omega_{Rb}(x, y, z) = 2\pi \cdot (23, 908, 911)$ Hz for ^{87}Rb and $\omega_{K}(x, y, z) = 2\pi \cdot (33, 1324, 1329)$ Hz for ^{41}K, respectively.

Here, the ^{87}Rb atoms are evaporatively cooled by removing the high-energetic atoms with a microwave knife and subsequent thermalization. Due to interspecies elastic collisions, the ^{41}K atoms are cooled sympathetically until both species finally form a BEC (Modugno et al. 2001). The microwave frequencies are chosen instead of the commonly used radio frequencies in single-species experiments to address only ^{87}Rb transitions in the evaporation process. The magnetic traps containing the condensates are moved to their final position, where the atoms are magnetically collimated to achieve ultralow expansion velocities. Subsequently, the atoms are prepared in the magnetically insensitive state $|F = 2, m_F = 0\rangle$ by microwave pulses and released into free fall. Due to the fast loading of the MOT and high thermalization rates on the atom chip trap, the formation of BECs is reached for both species after a few seconds, enabling many consecutive runs during the parabola flight.

Further information about the generation of BEC mixtures and the performance of the system with a ground-based test setup are given in (Piest 2021; Piest et al. 2019). A recent comparison of ground-based experiments with simulations reveals the influence of gravity on the ground state of the BEC mixture (Pichery et al. 2023).

Description of Apparatus

As shown in Fig. 1 (left) the scientific payload MAIUS-B (in red) is located on top of the two stages/engines of a VSB-30 sounding rocket. It offers a microgravity platform with residual accelerations in the 10^{-5} to 10^{-6}g range (Stamminger 2013) for about 325 s during a parabola flight. The onboard attitude control system reduces the residual rotations down to < 5 mrad/s (Becker et al. 2018).

In the following section, the scientific payload with its subsystems is presented in detail.

Payload Overview

In Fig. 1 (right) a detailed view of the scientific payload is shown. It is separated into five subsystems which constitute a full atom interferometer apparatus using BEC mixtures. The subsystems provide the necessary laser frequencies, electric currents for the manipulation of atoms as well as a thorough monitoring and housekeeping of the overall system. The subsystems are (from top to bottom): Electronics
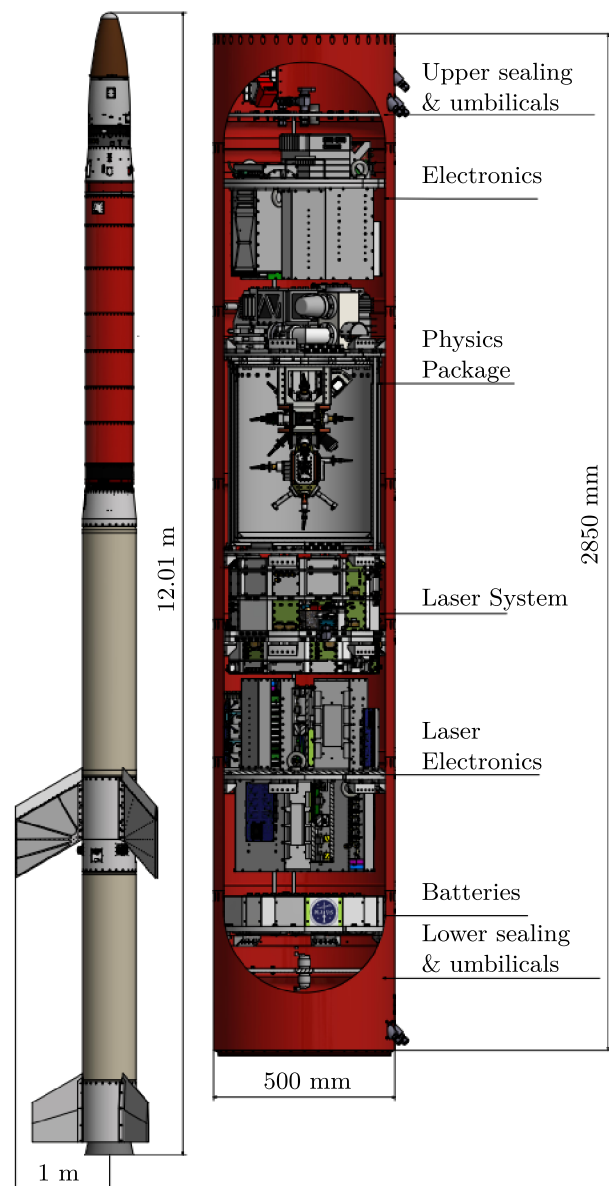
Fig. 1 The scientific payload (in red) on top of the two engines of a VSB-30 sounding rocket (left) and detailed view of the experimental payload (right). The payload hull is separated into seven RADAX segments. Image from Elsen (2023)

(EL), physics package (PP), laser system (LS), laser electronics (LE) and batteries (BA).

They are arranged in this order to place the center of gravity as close as possible (57 mm, according to CAD model) to the position of the atoms, considering the complete rocket without motors which will be separated after stage burn-out. Thus, during the experimental sequences no change in mass of the system is expected. Due to the position of the atoms close to the center-of-mass, any effects of residual rotations on the outcome of the atom interferometer are minimized. These effects may enter via a shift of the free ensemble

Table 1 Mass budget of the MAIUS-B payload

System	Mass in kg
Electronics	31.0
Physics Package	73.8
Laser System	53.5
Laser Electronics	35.2
Batteries	17.9
Cables & Cooling cycle	35.7
Sealing	8.1
Hull segments	80.1
SUM	335.3

position during the sequence or a differential phase shift of the interferometer arms due to the Coriolis force (Hogan et al. 2008; Lenef et al. 1997).

The rocket has a total length of 12 m including 2.8 m length of the scientific payload.

Since the experimental time in microgravity depends on the payload mass, it is essential to reduce it as much as possible. The mass budget presented in Table 1 with a total of 335.3 kg was obtained after a thorough optimization of the scientific payload design. It ensures a safe landing with the parachute system. Additionally, the manacle-ring, which connects the scientific payload to the rocket motor of the sounding rocket, withstands the expected loads during launch.

Each subsystem is suspended to the hull segments using six circularly arranged aluminum brackets. The brackets are equipped with two passive rubber vibration dampers and a safety bolt which limits the stretch of the dampers to prevent them from damage. Additionally, the bolts also serve as a safety measure in case of damper failure. Each suspension has to withstand static loads during ascent and re-entry of

up to 25 g and up to 100 g shock at touchdown. FEM simulations show a safety factor per suspension bracket of more than 1.4.

Physics Package

The PP is divided into two main sections, the pumping system to maintain the vacuum and the experimental chamber with its external components where the experiments are performed.

The pumping system includes an ion getter pump (IGP), a titanium sublimation pump (TSP) and a pressure sensor. It is seperated from the experimental chamber to protect it from magnetic stray fields originating from the IGP. To further reduce magnetic fields affecting the atoms, the experimental chamber is surrounded by a three-layer magnetic shield of Mu-metal with a measured shielding factor of 10000 and 2000 in lateral and longitudinal direction, respectively (Kubelka-Lange et al. 2016).

The experimental chamber inside the magnetic shield without the pumping system is shown in Fig. 2 (left). To separate the relatively high partial pressure area (source chamber) required for the efficient loading of the 2D-MOTs from the science chamber with a pressure in the 10^{-11} mbar regime, a two chamber design has been chosen. The two chambers are connected via a differential pumping stage (DPS) which maintains their pressure difference. Thus, the lifetime of the atomic ensembles in the science chamber can be increased due to less collisions with the background gas while maintaining a high atom flux from the source chamber.

As a reservoir, two ovens containing 1 g of Rb and K respectively are connected by a flange to the source chamber. The K oven is kept at a temperature of 46 °C while the
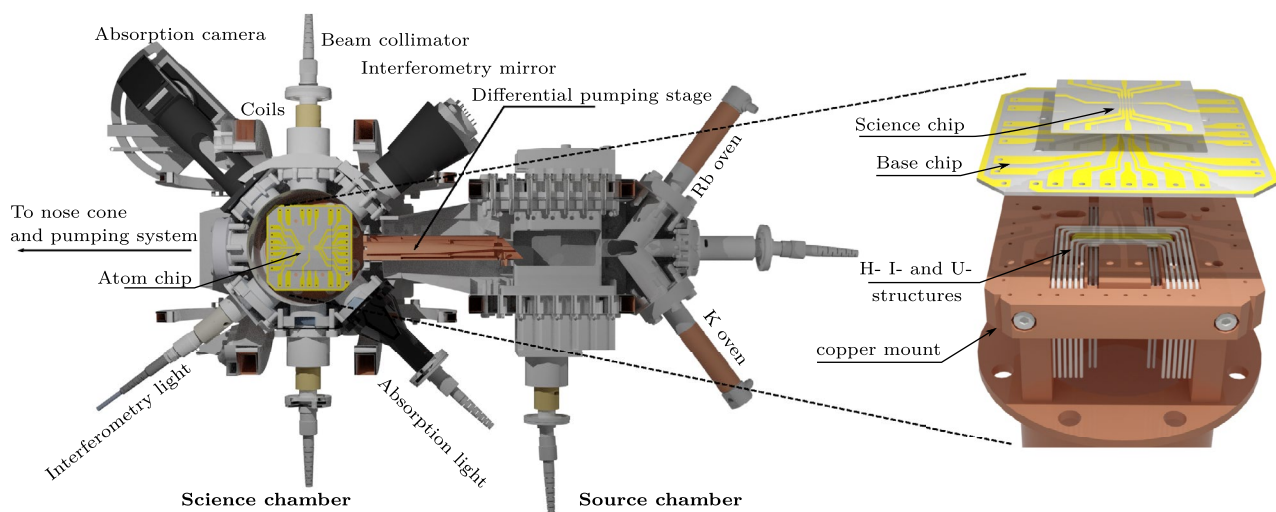
Fig. 2 Model of the experimental chamber (left) divided into science- and source chamber. Detailed view of the three-layer atom chip (right)

Rb oven is left unheated at room temperature. In the source chamber the K and Rb atoms are confined in a 2D-MOT which directs them through the DPS into the center of the science chamber.

To create high magnetic field gradients for atom trapping while keeping the switching times and current consumption low, an atom chip is mounted in the center of the science chamber, as shown in Fig. 2 (right). It consists of three layers: First, copper wires with a diameter of 1 mm in U-, I- and H-shapes are mounted onto the holder which can be used to generate high volume quadrupole field configurations for the MOT or harmonic magnetic traps. Above, a base chip with an electroplated z-shaped gold structure as well as two U-shaped loops for applying radio- or microwaves frequencies is glued. Glued on top of the base chip, a science chip with a 50μm wide z-shaped gold structure is closest to the atoms and allows for DC currents up to 2 A to create magnetic traps with high trapping frequencies. A mirror coating on top of the science chip allows for light configurations addressing the atoms from all directions. With the combination of these structures high volume as well as high frequency traps can be realized. Additional coils around both chambers produce offset fields in the science chamber and a quadrupole field in race-track configuration in the source chamber.

The light for cooling and manipulating the atoms is connected to the vacuum chamber via optical fibers and external optical setups to collimate and adjust the beams in diameter and shape.

Two perpendicular detection systems are used, one based on absorption imaging and the other one using the fluorescence of the atoms. With absorption imaging, the atom ensembles can be resolved using a CMOS camera (*FLIR Grasshopper GS3-U3-23S6M*). The frame rate of the camera can be increased up to 1178 Hz by reducing the region of interest of the sensor. With this technique, it is possible to detect both species separately by fast sequential imaging. Compared to a setup solely based on a photodiode, our setup allows for an in-depth analysis of the interaction-induced deformation of the mixture (Pichery et al. 2023), spatial interference patterns (Dickerson et al. 2013; Lachmann et al. 2021) and higher-order diffraction states (He et al. 2021). The fluorescence camera allows to observe the ensembles from an orthogonal direction, although its spatial resolution does not suffice to detect interference patterns.

For matter wave interferometry, a collimator (*Schäfter + Kirchhoff, 60FC-4-M15-37*) is attached to the vacuum chamber and retroreflected on the opposite side while passing through a quarter-wave plate twice. The vibrations of the interferometry mirror are monitored using an accelerometer (*Innalabs, Inn-202* (Innalabs 2011)) which is mounted rigidly behind the mirror.

Laser System

The laser system provides the light fields at 780 nm and 767 nm for the experiments with Rb and K, respectively. This light enables laser cooling and optical pumping of the atoms as well as atom interferometry and imaging of the BECs. Additionally, light for an optional optical dipole trap at 1064 nm is provided. The system is driven and controlled by the laser electronics and delivers light via eleven polarization maintaining (PM) fibers directly to the optical ports of the collimators at the PP. A photograph of the laser system is shown in Fig. 3. For a schematic overview of the optical setup we refer to (Mihm 2020). The system is assembled onto a 30 mm thick baseplate which also serves as the heatsink. It consists of five functional modules named (from bottom to top): beat-module, laser-module, reference-module, Zerodur-module and distribution-module. The laser light is generated directly at the required wavelengths of 780 nm, 767 nm and 1064 nm by micro-integrated diode lasers without the need of frequency-doubling, as it would be the case for lasers operating at telecom wavelength. The ten lasers are mounted onto both sides of the heatsink. Two of the ten laser modules are distributed feedback (DFB) lasers at 780 nm and 767 nm, which serve as reference lasers. The other eight laser modules are based on a master-oscillator-power-amplifier-configuration (MOPA) concept, where an extended cavity diode laser (ECDL) serves as the master oscillator and a semiconductor optical amplifier provides the power boost. Due to their narrower linewidth compared to DFB lasers, ECDLs are the most suitable choice in atom interferometry in order to minimize the impact of laser frequency noise on the phase sensitivity (Le Gouët et al. 2007).
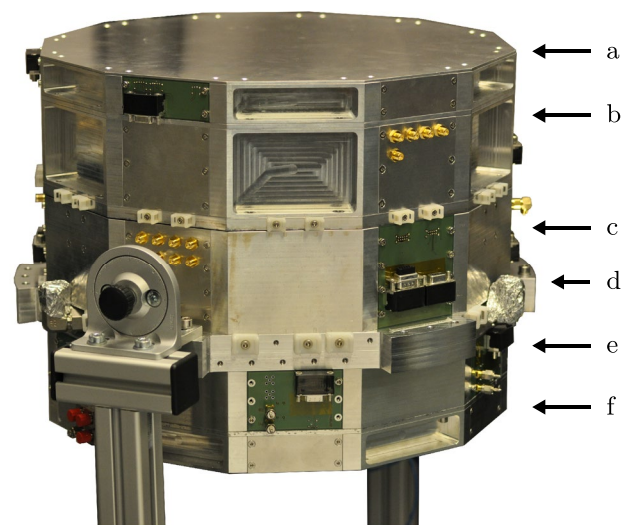
Fig. 3 Photograph of the laser system. **a** Distribution-module, **b** Zerodur-module, **c** reference-module, **d** heatsink, **e** laser-module, **f** beat-module

Each ECDL-MOPA laser provides more than 350 mW optical power ex fiber of spectral narrow light at 767 nm, 780 nm and 1064 nm, respectively (Wicht et al. 2017; Kürbis et al. 2020).

A single ECDL-MOPA laser emits at 1064 nm and provides light for the optical dipole trap. This laser is mounted in the reference module and is followed by a fiber pigtailed optical isolator mounted in the Zerodur-module, a fiber pigtailed acousto-optic modulator (AOM) for pulse shaping and a fiber switch to block residual light. The two DFB reference lasers are mounted onto the top side of the heatsink in the reference module. Each reference laser is frequency stabilized to the most prominent spectroscopy transitions of ^{85}Rb and ^{39}K, respectively, by means of modulation transfer spectroscopy (MTS) (Shirley 1982). The MTS setups are implemented in one spectroscopy module per species, which are based on a robust Zerodur assembly technology (Mihm et al. 2019; Duncker et al. 2014). Similar frequency references were previously used on sounding rocket missions (Lezius et al. 2016; Dinkelaker et al. 2017; Schkolnik et al. 2016).

Three ECDL-MOPAs emitting light at 780 nm and four ECDL-MOPAs at 767 nm are mounted in the laser-module onto the bottom side of the heatsink. They are frequency stabilized in the beat-module with respect to the reference lasers with a dynamic frequency offset. The main optical output power from the ECDL-MOPA modules operating at 780 nm and 767 nm is fiber coupled to five highly compact and robust optical benches. These consist of Zerodur-made baseplates with glued-on optics for low-loss beam manipulation in free space, including superposition of light of different wavelengths in the same polarization state with dichroic mirrors and laser pulse shaping with AOMs. The Zerodur-benches also feature mechanical shutters, built from metal blades fixed to the shaft of stepper motors, to block residual light that might harm the experiment when no light is required. From the Zerodur-benches, light is guided via PM optical fibers into the distribution module. Here, the light fields for laser cooling of both atomic species are finally overlapped and split in a fiber beam splitter array to provide the required beam balance. The light-grid pulses for Raman double-diffraction interferometry of Rb and K are also overlapped in a fiber beam splitter, before passing a fiber pigtailed AOM for common pulse shaping and a fiber switch for blocking residual light. From the distribution module, the light is finally guided to the PP via eleven PM optical fibers, each one connected to its respective collimator. Temperature sensitive components, such as ECDL-MOPAs or fiber beam splitters, are equipped with individual temperature control provided by the laser electronics. Multiple photodiodes and negative temperature coefficient (NTC) sensors allow for monitoring of the laser system's condition and troubleshooting. The five functional modules are connected via hinges to allow opening of the highly integrated system for maintenance if necessary. All fiber connections are spliced to minimize losses.

Electronics System

The electronic system consists of three subsystems, called batteries (BA), the laser electronics (LE) and general electronics (EL). They are all mounted on base plates which also serve as heatsinks within the TCS.

The grounding of all subsystems is defined by the BA. However, a second galvanically isolated circuit is defined by a set of batteries sitting in the EL supplying the chip- and coil current drivers. This minimizes any effects of ground shifts of the overall system to the atoms. Furthermore, the use of switching regulators has been avoided throughout the whole payload to comply with the required ultra-low noise performance for laser and atom-chip current drivers. Additionally, due to the high density of the payload, no efficient electromagnetic shielding of their high frequency noise is technically feasible.

In the following the three subsystems are discussed in more detail.

Batteries

The BA provides 24 outputs which distribute the voltages throughout the scientific payload. Each of these ports provide 6.6 V and 20 V and are controlled separately via the software. Furthermore, output currents and voltages are monitored for all ports. The power is delivered by LiFePO$_4$ batteries with 15 Ah each, assembled into two packs. The first pack has a 2S2P configuration with 6.6 V and the second pack has a 6S1P configuration with about 20 V. This leads to a possible autonomous operation time of 40 min of the overall system, which is sufficient for the parabola flight with additional temporal margin. The batteries can be charged with up to 20 A. To guarantee a safe operation, their charging and output currents are protected with 30 A fuses and the individual outputs to the experiment with 10 A fuses. Furthermore, the temperature within the module is monitored. In case of overheating, the charging current is additionally regulated by the firmware.

Laser Electronics

The LE delivers currents for lasers, generates the control loops for frequency stabilization and monitors laser frequencies. Additionally it synthesizes and amplifies radio frequencies (RF) to drive the AOMs and it contains a temperature control system to stabilize the temperature of the lasers and other sensitive optical components. It consists of two similar submodules mounted on opposite sides of the heatsink, one for the Rb and one for the K section of the lasersystem.

To allow for a modular assembly of scientific electronics, stackable cards similar to the PC/104 format form basic building blocks of the MAIUS-B electronic system. Each side of the LE contains two stacks formed by several cards. One of them contains current drivers for the power amplifier lasers, the other one current drivers for the diode lasers and their respective frequency controllers. The laser current drivers are designed to provide a low-noise current output up to 2 A in order to operate ECDL-MOPA systems or DFB lasers. The frequency controllers offer frequency stabilization of the reference lasers, control of frequency offsets between lasers and also allow for a phase lock loop (PLL) between two lasers. The latter is required to perform matter wave interferometry with light pulses based on Raman double-diffraction.

General Electronics

The EL supplies currents for the coils and for the atom chip structures of the PP. The chip and coil current drivers deliver up to 10 A and are configured together in one stack. To minimize heating and losses of the magnetically trapped atoms (Folman et al. 2002), they feature a low-noise current source. A second stack in this module houses the RF electronics and further auxiliary electronics. It generates microwave and RF signals needed for the evaporation and state preparation of the atoms. A dedicated atom chip protection module contains fuses and switching capabilities and additionally allows to monitor the currents delivered to the chip structures. The EL houses the main computer which stores the predefined experimental sequences. Furthermore, it is responsible for housekeeping and telemetry data processing.

Communication System

Communication between the different electronic stacks is based on a network made of polymer optical fibers which has shown to have a number of advantages compared to a more conventional Ethernet-based approach (Oberschulte et al. 2021). Besides the reduction of cable routing complexity and weight when using only a single wire, the use of plastic fibers also prevents ground loops between the connecting electronic components. The used protocol combines clock recovery, in-band signaling, data transfer and prioritized trigger delivery over a single fiber. The raw signal at 150 MHz enables clock recovery and data transfer at 50 MHz. For in-band signaling and error detection 8b/10b line code is used as a transport-level protocol (Widmer and Franaszek 1983). On network layer four nibbles in each packet are used for the routing through the network from master nodes to endpoints with up to four hops. A single packet can be indefinitely long: Beginning and end are signaled by 8b/10b control words. Congestion is prevented by

feedback control signals which temporarily stop the data flow in case of full buffers at the receiving end. For the experiments simultaneous execution of programmed actions at the endpoints is important. Thus, a special, prioritized symbol is used as a global trigger; it will be transferred to all endpoints with a deterministic delay.

Software

The general architecture of the software inherits from the concepts initially developed for the MAIUS-1 mission (Weps et al. 2018). It consists of three main components: the experiment control software (ECS), the experiment design tools (EDT) and the ground control software (GCS) which are described below in detail. The ECS is running on the onboard computer installed in the sounding rocket. It has direct communication with the experiment control electronics which perform the real-time execution of experiments. As the software doesn't need to handle real-time it runs in an Ubuntu Linux environment. For communication with the electronics the TCP/IP protocol via Ethernet is used which is then bridged to the optical fiber network. On the other side, it uses the RF link of the rocket to directly communicate with the ground software. The task of the ECS is to control the experiment execution as well as collecting telemetry from the different subsystems. Due to the large amount of hardware and domains involved, the software development is supported through a model-driven approach. This model-driven approach covers the drivers for the control electronics as well as the experiments the software shall execute. A minimal core system is manually implemented in the C++ programming language. C++ offers high performance which is needed due to the limited amount of resources on the onboard computer. Furthermore, compared to the C programming language, it allows better code organization through object orientation. The hardware and the experiments are provided as high-level descriptions by engineers and scientists using self-developed domain-specific languages (DSLs). In case of the hardware, the DSL description is used to generate C++ code which is then compiled with the rest of the ECS. For the experiments the DSL description is based on YAML ain't markup language (YAML) which is interpreted and executed onboard during flight. Two main descriptions, called sequences and graphs, have been created to describe the experiments conducted during flight. Sequences are abstract descriptions of single experiments. Graphs are shaped as decision trees and use sequences as basic blocks. They allow a dynamic execution of the sequences depending on the outcome of previous experiments. The EDT comprise the components used by the experimentalists in order to create or monitor experiments. For this, different graphical user interfaces allow to create new sequences and graphs in a convenient way. Also,

machine learning algorithms are implemented to optimize the experimental parameters (Wigley et al. 2016). Finally, the GCS is the set of applications running on the ground stations from where the mission will be controlled and monitored. It allows communication of telecommands and telemetry with the ECS using a central telemetry and telecommand (TMTC) service. The TMTC forwards telecommands from the ground stations and distributes the telemetry received from the ECS. Thus, it is possible to upload sequences and visualize and store telemetry during flight. However, the execution of the experiments is expected to be fully autonomous.

Thermal Control System and Ground Support Equipment

The TCS of the MAIUS-B apparatus takes two operation modes into account, the laboratory and flight mode. In laboratory operation the payload is actively cooled via the connected ground support equipment (GSE) and all components which produce heat within the payload are considered. During ascent and re-entry aerodynamic drag adds a further heat source to the system. However, no active cooling is possible and the design of the TCS in flight mode relies solely on the thermal mass. For the flight, only conduction is assumed since natural convection does not occur in microgravity.

The estimated internally produced thermal loads are presented in Table 2. Each subsystem except for the PP is equipped with an active liquid cooling with the respective baseplates acting as heatsinks. The design of the heatsinks for EL, LS, and LE include two base plates screwed together. A meander is mounted inside these base plates and is connected to the intermodule coolant hoses. The base plate of the PP is not equipped with liquid cooling. Nevertheless, to support an efficient heat transfer of heat-producing amplifiers sitting on top of the PP, these are connected to an additional liquid cooled plate. With a comparatively low heat load of 28.8 W the heatsink of the BA is made of a single-layer base plate with a meander mounted below.

We performed a ground-based flight simulation to test the functionality of the payload without external cooling. During this test, the payload was able to operate for 25 min
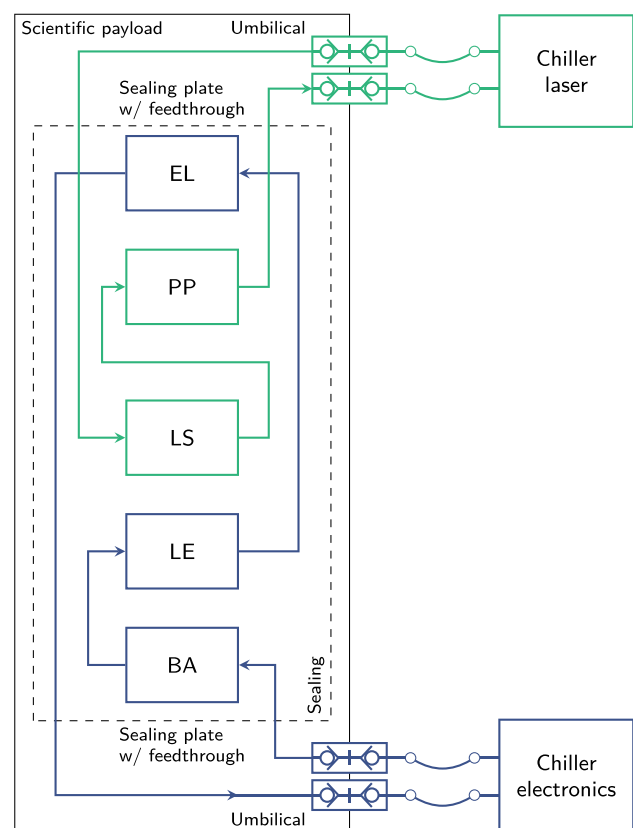
within its temperature limits. The temperature of the laser system and electronics heatsink was rising from 19.0 °C to 24.2 °C and from 19.0 °C to 24.7 °C, respectively. The hull segments were not heated to mimic the aerodynamic drag during flight. Nevertheless, we expect a minor influence due to measurements in the flight of MAIUS-1 (Grosse et al. 2019). The expected system operating time from active cooling disconnection, including launch, to re-entry is 16 min. The test results therefore indicate a safe flight operation within a sufficient temperature margin.

The TCS is divided into two cooling cycles which are connected via umbilicals to the GSE, as shown in Fig. 4. A *Huber Unichiller 007* is used for the laser cycle and a *Huber Unichiller 010* for the electronic subsystems. These chillers provide a maximum flow rate of 25L/min and allow for pressure loss compensation of up to 2.5bar. In laboratory operation, the TCS with its two chillers is able to continuously stabilize the temperature of the payload as required, compensating for all internal heat loads listed in Table 2.

Since the GSE is placed on the launch pad within the exhaust gas of the rocket, the chiller is integrated into metal cases. These cases are made of aluminum and will

System	Heat load in W
Electronics	174.0
Physics Package	63.9
Laser System	100.0
Laser Electronics	340.9
Batteries	28.8
SUM	707.6

Table 2 Internal heat loads of the MAIUS-B apparatus

Fig. 4 Schematic overview of the two cycle cooling concept within the TCS. The electronics cycle (in blue) feeds the subsystems BA, LE and EL and the laser cycle (in green) the LS and PP. Figure adapted from Elsen (2023)

be covered with a fire resistant pyroblanket to withstand the rough conditions inside the launch tower. Due to the low ambient temperature at the launch site/landing area and to avoid damage caused by freezing of the remaining cooling liquid inside the payload, a thermo fluid (glycol/water mixture) is used. The mixture with 44% of glycol prevents freezing down to −30 °C and a mixture with 52% glycol down to −40 °C. This, however results in a higher viscosity of the cooling liquid as discussed in "Flow Rate Measurement" section.

Umbilicals and Sealing

After the subsystems are integrated in flight configuration into the hull segments, the payload needs to be accessible for coolant, power and data connection. Several umbilicals are connected until lift-off to ensure active liquid cooling of the TCS, monitor and charge the batteries, enable data transfer, and allow an activation of the TSPs within the PP. As shown in Fig. 5, the quick connectors are equipped with a lanyard steel cable which will be attached to the launch pad. This will unlock the plug automatically by the pull of the rocket as it lifts off during launch.

The payload is pressurized with artificial air to ensure a constant and reproducible environment for the LS. To this end, it is sealed with sealing plates on the bottom and top hull segments using rubber O-rings. The seven hull segments (cf. Fig. 1) are connected to each other by standardized RADAX flanges, also sealed with rubber O-rings. To pressurize the payload, both sealing plates are equipped with a *Swagelok* bulkhead fitting and ball tap as well as further feedthroughs for liquid cooling and power/data connection. All power and data connections use hermetic military

grade connectors. Cables and hoses from the umbilical to the GSE need to withstand the high temperatures during launch. Thus, these lines are equipped with a fire protection which is rated up to 200 °C.

Qualification Process

The qualification process starts with pressuring tests of the hull segments to verify the integrity of the sealed payload compartment. Moreover the TCS is tested by measuring the flow rate of the cooling liquid and simulated via finite-element method (FEM) analysis. Furthermore, random frequency vibration tests on component and subsystem level are conducted. Prior to flight campaign, the overall payload in launch configuration requires additional tests including a bench test, a spin balance test and further vibration tests. In the following sections these tests are discussed in more depth.

Payload Pressuring Test

To measure the pressure loss over time, the hull segments including the sealing plates prepared in flight configuration are pressurized with artificial air (20% oxygen and 80% nitrogen). To simulate the conditions during the actual flight, where the pressure difference between the outside (vacuum) and the inside of the payload (atmospheric pressure) will be around 1000 - 1100 hPa, the payload will be pressurized to an absolute pressure of 2100 hPa. The pressure is monitored and logged for 90 h. During the measurement, a pressure loss of 40 hPa has been detected. The same sealing concept was used for the MAIUS-A payload, where no leakages were observed during the flight mission (Grosse et al. 2019). Thus, we don't expect any significant leakages before and during the upcoming flights.

Flow Rate Measurement

For the TCS and as an input for thermal simulations it is important to measure the flow rate of the cooling cycles. In general, a higher viscosity of the cooling liquid leads to a reduction of the flow rate. A too small flow rate could possibly cause problems in transporting heat out of the system. The viscosity of glycol at room temperature is 21 times higher compared to water (Tsierkezos and Molinou 1998). Therefore, two different glycol-water mixtures are tested (44% and 52% glycol) to measure the effect of the higher viscosity. To measure the flow rate of the chiller without the cooling cycle as a reference, a test with a flow rate sensor and two short connection hoses (0.8 m each) is set up. The test shows a flow rate of 6.4 L/min.

Water umbilical   Power umbilical
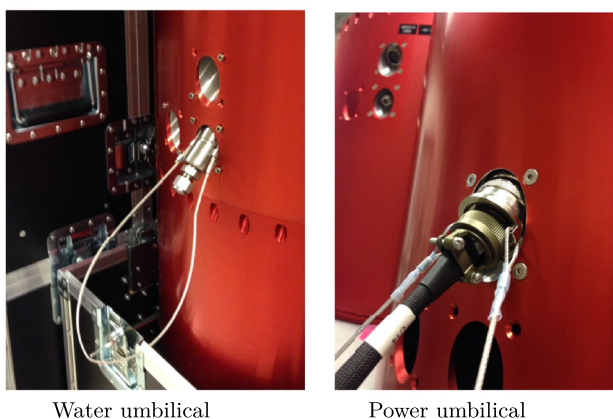
Fig. 5 Coolant (left) and power umbilicals (right). The umbilicals for coolant liquid are equipped with a *Swagelok* quick-coupling. The electrical umbilicals use push-and-pull quick connectors from *Souriau*. Both are mounted at the upper and lower hull segments. Picture from Grosse (2016)

To simulate a realistic setup of a single cooling cycle without the subsystems being included, the length of the cooling hoses within the hull is augmented to 21 m including similar amount of fittings. Further, the inlet and outlet of the chiller are connected with the actual hoses as shown in Fig. 6. On the opposite side, both hoses are mounted to the upper umbilicals to simulate the most disadvantageous configuration. The flow rate sensor is connected with two 0.8 m hoses directly to the lower coolant umbilicals. As a result, flow rates of up to 5.2 L/min (44% glycol) and 4.8 L/min (52% glycol) are measured. This shows that the percentage of glycol has a direct impact on the flow rate. Nevertheless, FEM simulations based on these results show that the flow rate is sufficient to operate the TCS.

Fig. 6 Flow rate test of the cooling cycles of MAIUS-B. The case which houses the chiller is placed right next to the scientific payload (red hull segments). The orange hoses are equipped with a fire protection to avoid damage during launch. Picture from Elsen (2023)

Vibration Tests

A sequential vibration qualification on component, subsystem and payload level throughout the technology life cycle is approached in this project. All vibration tests are conducted for a duration of 60 s for all three axes in a frequency range of $20 - 2000$ Hz. Within component level, all critical parts are tested hard-mounted with a root mean square (RMS) value of 8.1 g to minimize the risk of a failure during following subsystem or payload level tests. The subsystem level tests were performed in a cylindrical shaker adapter using the identical mounting as in the hull segments including a vibration isolation. The qualification on subsystem level is achieved with the vibration test profile given in Table 3. The actual vibrational loads during flight are expected to be one-third of the qualification level (Grosse 2016). Before and after each random test a resonance sine frequency sweep from 5 Hz to 2000 Hz with an amplitude of 0.25 g and a sweep rate of 2 Oct/min is performed. By comparing the measured frequency responses of the payload during the two resonance runs the test specimen are screened for structural flaws.

Above structural changes, further system specific parameters or functions have been monitored and checked for degradation or malfunction due to vibrational loads. For the laser system, parameters like optical powers along the various beampaths including coupling efficiencies and the alignment of optical components are of particular interest.

In case of the physics package, the vacuum pressure is a critical test parameter, which should be in the range of 10^{-10} mbar. Such an ultra-high vacuum pressure is required by the experiments for the efficient BEC production and atom interferometry. Throughout the vibration tests, the vacuum system was able to comply with this requirement. Also the effect of the vibrations on the vapour pressure of ^{87}Rb within the source chamber is probed. Results for the longitudinal vibration profile are shown in Fig. 7. The vapour pressure is measured spectroscopically by monitoring the absorbed light due to the D2-transition which is scanned by an external spectroscopy laser. Given the number of

Table 3 Random vibration test profiles on subsystem level with power spectral density (PSD) and RMS values

Lateral		Longitudinal	
Frequency in Hz	PSD in g^2/Hz	Frequency in Hz	PSD in g^2/Hz
20 - 400	0.002	20 - 900	0.002
400 - 600	0.03	900 - 1600	0.01
600 - 1300	0.002	1600 - 1800	0.06
1300 - 2000	0.03	1800 - 2000	0.03
RMS Value	5.41 g	RMS Value	5.18 g
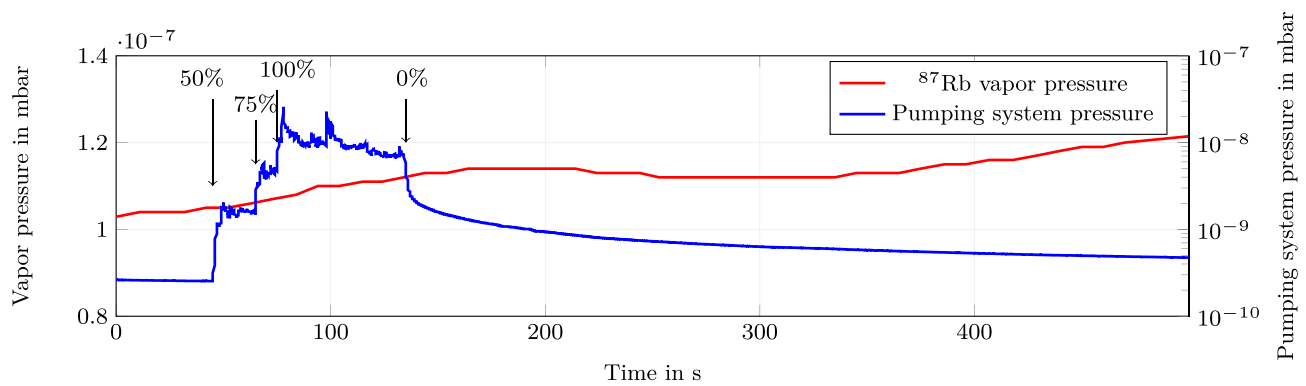
Fig. 7 Vacuum pressure in PP pumping system (blue curve) and ^{87}Rb vapour pressure in the source chamber (red curve) prior, during and after vibrational test of the longitudinal axis. The rms-value of vibra-

tion loads is increased to the final value in three steps, as indicated by the arrows. Figure adapted from Piest (2021)

absorbing atoms and the temperature of the source chamber, the vapour pressure can be inferred by using the ideal gas law. The observed rise of the vapour pressure can not necessarily be attributed to the vibrations due to additional heat transfer from the vibration table and air condition to the experiment. However, it could be demonstrated that no significant increase, decrease or jumps of the vapour pressure are expected after rocket launch which could alter the atomic flux during flight experiments.

At the time we performed the vibration tests, the measured vacuum pressure was in the low 10^{-10} mbar regime which is an order of magnitude above the current value. The expected lifetime of magnetically trapped Rb or K due to background gas collisions with hydrogen molecules is in the order of several seconds for a background pressure of 10^{-9} mbar (Folman et al. 2002). Due to the much better vacuum conditions at present, it is expected that these results will be outperformed by future vibration tests.

All subsystems were successfully vibration tested and qualified for the flight onboard the MAIUS-B sounding rocket.

Summary and Outlook

A payload for parabolic flights on a VSB-30 sounding rocket is presented which is able to generate ultracold mixtures of ^{41}K and ^{87}Rb and perform matter wave interferometry in microgravity. The apparatus consists of five modules which condense the functionality of a lab filling setup into the challenging constraints of a sounding rocket. To allow an autonomous operation during the parabolic flight, the software executes a graph which determines the chronology of experimental sequences based on a decision tree. To cope with the expected heat load of approximately 708 W, the TCS is designed to actively cool the experiment in laboratory operation and passively during flight. All subsystems are expected

to withstand the static and dynamic loads and work within the operational requirements during launch and re-entry which has been demonstrated in dedicated vibration tests.

To test the functional interaction of the payload in its final configuration during flight, further qualification tests are going to be carried out: In the bench test all payload systems including the scientific payload, the recovery system, the ignition unit, the attitude control system, and service module are brought together and are operated in flight like configuration. Its aim is to screen for interferences between the payload systems, test the on-board software and to train the personnel in the procedures performed prior to and during flight.

The spin and balance test is a procedure to ensure the stability of the payload during ascent. Here, the payload is rotated with up to 2 Hz along its longitudinal axis to determine static and dynamic unbalances from the forces observed, which are compensated by installing counter weights. The maximal rotation rate during ascent of the rocket is expected to be 2.7 Hz, thus the mechanical stability of the payload components under flight-like conditions is also tested during spin balancing.

The findings of the planned experiments aboard the MAIUS-2/3 missions will advance the knowledge of the physics of ultracold quantum gases in microgravity. Further, a successful mission presents a technological milestone for possible future applications of cold quantum gases in orbital platforms including inertial sensing, space geodesy up to gravitational wave detection.

Author Contributions Michael Elsen and Baptist Piest wrote the manuscript, with contributions from all authors. Michael Elsen, Baptist Piest, Oliver Anton, Paweł Arciszewski, Wolfgang Bartosch, Dennis Becker, Jonas Böhm, Sören Boles, Klaus Döringshoff, Jens Grosse, Priyanka Guggilam, Ortwin Hellmig, Isabell Imwalle, Simon Kanthak, Christian Kürbis, Maike Diana Lachmann, Moritz Mihm, Alexandros Papakonstantinou, Christian Reichelt, Marvin Warner, Thijs Wendrich and André Wenzlawski designed, built and tested the apparatus. Fabian Adam, Paweł Arciszewski, Kai Bleeke, Matthias Koch, Hauke Müntinga, Ayush Mani Nepal, Tim Obertschulte, Peter Ohr, Arnau Prat, Jan Sommer and Christian Spindeldreier developed and implemented the software. Claus Braxmaier, Holger Blume, Daniel Lüdtke, Achim Peters, Ernst Maria Rasel, Klaus Sengstock, Andreas Wicht and Patrick Windpassinger are the co-principal investigators of the project, and Jens Grosse is principal investigator.

Availability of Data and Material Corresponding contact Michael Elsen.

Code Availability Not applicable.

Declarations

Ethics Approval The authors confirm that the manuscript is original and has not been published elsewhere or is it currently under consideration for publication elsewhere.

Consent to Participate Not applicable.

Consent for Publication All authors provided the consent for publication.

Conflict of Interest The authors declare that they have no conflict of interest.

References

Aguilera, D.N., Ahlers, H., Battelier, B., Bawamia, A., Bertoldi, A., Bondarescu, R., Bongs, K., Bouyer, P., Braxmaier, C., Cacciapuoti, L., Chaloner, C., Chwalla, M., Ertmer, W., Franz, M., Gaaloul, N., Gehler, M., Gerardi, D., Gesa, L., Gürlebeck, N., Hartwig, J., Hauth, M., Hellmig, O., Herr, W., Herrmann, S., Heske, A., Hinton, A., Ireland, P., Jetzer, P., Johann, U., Krutzik, M., Kubelka, A., Lämmerzahl, C., Landragin, A., Lloro, I., Massonnet, D., Mateos, I., Milke, A., Nofrarias, M., Oswald, M., Peters, A., Posso-Trujillo, K., Rasel, E., Rocco, E., Roura, A., Rudolph, J., Schleich, W., Schubert, C., Schuldt, T., Seidel, S., Sengstock, K., Sopuerta, C.F., Sorrentino, F., Summers, D., Tino, G.M., Trenkel, C., Uzunoglu, N., von Klitzing, W., Walser, R., Wendrich, T., Wenzlawski, A., Weßels, P., Wicht, A., Wille, E., Williams, M., Zahzam, P.W.N.: STE-QUEST–test of the universality of free fall using cold atom interferometry. Classical Quantum Gravity **31**(11) (2014). https://doi.org/10.1088/0264-9381/31/11/115010

Ahlers, H., Leonardo, B., Bassi, A., Battelier, B., Beaufils, Q., Bongs, K., Bouyer, P., Braxmaier, C., Buchmueller, O., Carlesso, M., E Charron, M.L.C., Corgier, R., Donadi, S., Droz, F., Ecoffet, R., Ellis, J., Estève, F., Gaaloul, N., Gerardi, D., Giese, E., Grosse, J., Hees, A., Hensel, T., Herr, W., Jetzer, P., Kleinsteinberg, G., Klempt, C., Lecomte, S., Lopes, L., Loriani, S., Métris, G., Martin, T., Martín, V., Müller, G., Nofrarias, M., Santos, F.P.D., Rasel, E.M., Robert, A., Saks, N., Salter, M., Schlippert, D., Schubert, C., Schuldt, T., Sopuerta, C.F., Struckmann, C., Tino, G.M., Valenzuela, T., von Klitzing, W., Wörner, L., Wolf, P., Yu, N., Zelan, M.: Ste-quest: Space time explorer and quantum equivalence principle space test. Preprint at arXiv: 2211.15412 (2022)

Alonso, I., Alpigiani, C., Altschul, B., Araújo, H., Arduini, G., Arlt, J., Badurina, L., Balaž, A., Bandarupally, S., Barish, B.C., et al.: Cold atoms in space: community workshop summary and proposed road-map. EPJ Quantum Technology **9**(1), 1–55 (2022)

Ammann, H., Christensen, N.: Delta Kick cooling: a new method for cooling atoms. Phys. Rev. Lett. **78**(11), 2088–2091 (1997). https://link.aps.org/doi/10.1103/PhysRevLett.78.2088

Asenbaum, P., Overstreet, C., Kim, M., Curti, J., Kasevich, M.A.: Atom-interferometric test of the equivalence principle at the 10^{-12} level. Preprint at arXiv:2005.11624 (2020)

Becker, D., Lachmann, M.D., Seidel, S.T., Ahlers, H., Dinkelaker, A.N., Grosse, J., Hellmig, O., Müntinga, H., Schkolnik, V., Wendrich, T., Wenzlawski, A., Weps, B., Corgier, R., Franz, T., Gaaloul, N., Herr, W., Lüdtke, D., Popp, M., Amri, S., Duncker, H., Erbe, M., Kohfeldt, A., Kubelka-Lange, A., Braxmaier, C., Charron, E., Ertmer, W., Krutzik, M., Lämmerzahl, C., Peters, A., Schleich, W.P., Sengstock, K., Walser, R., Wicht, A., Windpassinger, P., Rasel, E.M.: Space-borne Bose-Einstein condensation for precision interferometry. Nature **562**(7727), 391–395 (2018)

Berg, P., Abend, S., Tackmann, G., Schubert, C., Giese, E., Schleich, W.P., Narducci, F.A., Ertmer, W., Rasel, E.M.: Composite-light-pulse technique for high-precision atom interferometry. Phys. Rev. Lett. **114**(063002) (2015)

Carollo, R.A., Aveline, D.C., Rhyno, B., Vishveshwara, S., Lannert, C., Murphree, J.D., Elliott, E.R., Williams, J.R., Thompson, R.J., Lundblad, N.: Observation of ultracold atomic bubbles in orbital microgravity. Nature **606**, 281–286 (2022)

Condon, G., Rabault, M., Barrett, B., Chichet, L., Arguel, R., Eneriz-Imaz, H., Naik, D., Bertoldi, A., Battelier, B., Bouyer, P., Landragin, A.: All-Optical Bose-Einstein Condensates in Microgravity. Phys. Rev. Lett. **123**(240402) (2019)

Corgier, R., Amri, S., Herr, W., Ahlers, H., Rudolph, J., Guery-Odélin, D., Rasel, E.M., Charron, E., Gaaloul, N.: Fast manipulation of Bose-Einstein condensates with an atom chip. New. J. Phys. **20**(5), 055002 (2018). http://dx.doi.org/10.1088/1367-2630/aabdfc

Corgier, R., Loriani, S., Ahlers, H., Posso-Trujillo, K., Schubert, C., Rasel, E.M., Gaaloul, N.: Interacting quantum mixtures for precision atom interferometry. New. J. Phys. **22**(123008) (2020)

Deppner, C., Herr, W., Cornelius, M., Stromberger, P., Sternke, T., Grzeschik, C., Grote, A., Rudolph, J., Herrmann, S., Krutzik, M., Wenzlawski, A., Corgier, R., Charron, E., Guéry-Odelin, D., Gaaloul, N., Lämmerzahl, C., Peters, A., Windpassinger, P., Rasel, E.M.: Collective-mode enhanced matter-wave optics. Phys. Rev. Lett. **127**, 100401 (2021)

Dickerson, S.M., Hogan, J.M., Sugarbaker, A., Johnson, D.M.S., Kasevich, M.A.: Multiaxis inertial sensing with long-time point source atom interferometry. Phys. Rev. Lett. **111**(083001) (2013)

Dinkelaker, A.N., Schiemangk, M., Schkolnik, V., Kenyon, A., Lampmann, K., Wenzlawski, A., Windpassinger, P., Hellmig, O., Wendrich, T., Rasel, E.M., Giunta, M., Deutsch, C., Kürbis, C., Smol, R., Wicht, A., Krutzik, M., Peters, A.: Autonomous frequency stabilization of two extended-cavity diode lasers at the potassium wavelength on a sounding rocket. Appl. Opt. **56**(5), 1388–1396 (2017)

Duncker, H., Hellmig, O., Wenzlawski, A., Grote, A., Rafipoor, A.J., Rafipoor, M., Sengstock, K., Windpassinger, P.: Ultrastable, Zerodur-based optical benches for quantum gas experiments. Appl. Opt. **53**(20), 4468–4474 (2014)

Elsen, M.: Ultra-high vacuum systems for experiments with cold atoms in space. (2023). https://doi.org/10.26092/elib/2382

Folman, R., Krüger, P., Schmiedmayer, J., Denschlag, J., Henkel, C.: Microscopic atom optics: From wires to an atom chip. Adv. At. Mol. Phys. **48** (2002). https://doi.org/10.1016/S1049-250X(02)80011-8

Frye, K., Abend, S., Bartosch, W., Bawamia, A., Becker, D., Blume, H., Braxmaier, C., Chiow, S.W., Efremov, M.A., Ertmer, W., Fierlinger, P., Gaaloul, N., Grosse, J., Grzeschik, C., Hellmig, O., Henderson, V.A., Herr, W., Israelsson, U., Kohel, J., Krutzik, M., Kürbis, C., Lämmerzahl, C., List, M., Lüdtke, D., Lundblad, N., Marburger, J.P., Meister, M., Mihm, M., Müller, H., Müntinga, H., Oberschulte, T., Papakonstantinou, A., Perovšek, J., Peters, A., Prat, A., Rasel, E.M., Roura, A., Schleich, W.P., Schubert, C., Seidel, S.T., Sommer, J., Spindeldreier, C., Stamper-Kurn, D., Stuhl, B.K., Warner, M., Wendrich, T., Wenzlawski, A., Wicht, A., Windpassinger, P., Yu, N., Wörner, L.: The Bose-Einstein condensate and cold atom laboratory. EPJ. Quantum. Technol. **8**, 1 (2021). https://doi.org/10.1140/epjqt/s40507-020-00090-8

Gaaloul, N., Meister, M., Corgier, R., Pichery, A., Boegel, P., Herr, W., Ahlers, H., Charron, E., Williams, J.R., Thompson, R.J., Schleich, W.P., Rasel, E.M., Bigelow, N.P.: A space-based quantum gas laboratory at picokelvin energy scales. Nat. Comm. **13**(7889) (2022)

Grosse, J.: Thermal and mechanical design and simulation for the first high precision quantum optics experiment on a sounding rocket. (2016)

Grosse, J., Elsen, M., Braxmaier, C., the QUANTUS team.: Lessons learned from the first flight of an atom interferometer payload on a vsb-30 sounding rocket). In: Proceedings of the 24th ESA Symposium on European Rocket and Balloon Programmes and Related Research. (2019)

Hartmann, S., Jenewein, J., Giese, E., Abend, S., Roura, A., Rasel, E.M., Schleich, W.P.: Regimes of atomic diffraction: Raman versus Bragg diffraction in retroreflective geometries. Phys. Rev. A **101**(053610) (2020). https://doi.org/10.1103/PhysRevA.101.0536105

He, M., Chen, X., Fang, J., Ge, G., Li, J., Zhang, D., Zhou, L., Wang, J., Zhans, M.: Phase shift of double-diffraction Raman interference due to high-order diffraction states. Phys. Rev. A **103**(063310) (2021)

Hogan, J.M., Johnson, D., Kasevich, M.A.: Light-pulse atom interferometry. Preprint at arXiv:0806.3261v1 (2008)

Innalabs.: Quartz Accelerometer INN-202, Datasheet (2011)

Kubelka-Lange, A., Herrmann, S., Grosse, J., Lämmerzahl, C., Rasel, E.M., Braxmaier, C.: A three-layer magnetic shielding for the MAIUS-1 mission on a sounding rocket. Rev. Sci. Instr. **87**(6), 063101 (2016)

Kürbis, C., Bawamia, A., Krüger, M., Smol, R., Peters, A., Wicht, A., Tränkle, G.: Extended cavity diode laser master-oscillator-power-amplifier for operation of an iodine frequency reference on a sounding rocket. Appl. Opt. **59**(2), 253 (2020). https://doi.org/10.1364/ao.379955

Lachmann, M.D., Ahlers, H., Becker, D., Dinkelaker, A.N., Grosse, J., Hellmig, O., Müntinga, H., Schkolnik, V., Seidel, S.T., Wendrich, T., Wenzlawski, A., Carrick, B., Gaaloul, N., Lüdtke, D., Braxmaier, C., Ertmer, W., Krutzik, M., Lämmerzahl, C., Peters, A., Schleich, W.P., Sengstock, K., Wicht, A., Windpassinger, P., Rasel, E.M.: Ultracold atom interferometry in space. Nat. Comm. **12**(1317) (2021). https://doi.org/10.1038/s41467-021-21628-z

Le Gouët, J., Cheinet, P., Kim, J., Holleville, D., Clairon, A., Landragin, A., Santos, F.P.D.: Influence of lasers propagation delay on the sensitivity of atom interferometers. Eur. Phys. J. D. **44**(419-425) (2007)

Lenef, A., Hammond, T.D., Smith, E.T., Chapman, M.S., Rubenstein, R.A., Pritchard, D.E.: Rotation Sensing with an Atom Interferometer. Phys. Rev. Lett. **78**(760) (1997)

Leveque, T., Gauguet, A., Michaud, F., Santos, F.P.D., Landragin, A.: Enhancing the area of a Raman atom interferometer using a versatile double-diffraction technique. Phys. Rev. Lett. **103**(080405) (2009). https://doi.org/10.1103/PhysRevLett.103.080405

Lezius, M., Wilken, T., Deutsch, C., Giunta, M., Mandel, O., Thaller, A., Schkolnik, V., Schiemangk, M., Dinkelaker, A., Kohfeldt, A., Wicht, A., Krutzik, M., Peters, A., Hellmig, O., Duncker, H., Sengstock, K., Windpassinger, P., Lampmann, K., Hülsing, T., Hänsch, T.W., Holzwarth, R.: Space-borne frequency comb metrology. Optica **3**(12), 1381–1387 (2016)

Liu, L., Lü, D.S., Chen, W.B., Li, T., Qu, Q.Z., Wang, B., Li, L., Ren, W., Dong, Z.R., Zhao, J.B., Xia, W.B., Zhao, X., Ji, J.W., Ye, M.F., Sun, Y.G., Yao, Y.Y., Song, D., Liang, Z.G., Hu, S.J., Yu, D.H., Hou, X., Shi, W., Zang, H.G., Xiang, J.F., Peng, X.K., Wang, Y.Z.: In-orbit operation of an atomic clock based on laser-cooled 87Rb atoms. Nature Comm. **9**(2760) (2018). https://doi.org/10.1038/s41467-018-05219-z

Loriani, S., Schlippert, D., Schubert, C., Abend, S., Ahlers, H., Ertmer, W., Rudolph, J., Hogan, J., Kasevich, M., Rasel, E.M., Gaaloul, N.: Atomic source selection in space-borne gravitational wave detection. New. J. Phys. **21**(063030) (2019). https://doi.org/10.1088/1367-2630/ab22d0

Lévêque, T., Fallet, C., Lefebve, J., Piquereau, A., Gauguet, A., Battelier, B., Bouyer, P., Gaaloul, N., Lachmann, M., Piest, B., Rasel, E., Müller, J., Schubert, C., Beaufils, Q., Santos, F.P.D.: Carioqa: Definition of a quantum pathfinder mission. Preprint at arXiv:2211.01215 (2022)

Mihm, M.: Laser System Technology for Quantum Experiments in Space and beyond (2020)

Mihm, M., Marburger, J.P., Wenzlawski, A., Hellmig, O., Anton, O., Döringshoff, K., Krutzik, M., Peters, A., Windpassinger, P.: Acta Astronautica ZERODUR ® based optical systems for quantum gas experiments in space. Acta Astronautica **159**(February), 166–169 (2019). https://doi.org/10.1016/j.actaastro.2019.03.060

Modugno, G., Ferrari, G., Roati, G., Brecha, R.J., Simoni, A., Inguscio, M.: Bose-Einstein condensation of potassium atoms by sympathetic cooling. Science **294**(5545) (2001)

Oberschulte, T., Wendrich, T., Blume, H.: FPGA-based low-cost synchronized fiber network for experimental setups in space. J. Instrum. **16**(11), P11016 (2021)

Pichery, A., Meister, M., Piest, B., Böhm, J., Rasel, E.M., Charron, E., Gaaloul, N.: Efficient numerical description of the dynamics of interacting multispecies quantum gases. Preprint at arXiv:2305.13433 (2023)

Piest, B.: Bose-Einstein condensation of K-41 and Rb-87 on an atom chip for sounding rocket missions. (2021)

Piest, B., Lachmann, M.D., Anton, O., Bartosch, W., Becker, D., Böhm, J., Döringshoff, K., Elsen, M., Grosse, J., Kürbis, C., Mihm, M., Popp, M., Wendrich, T., Wenzlawski, A., Braxmeier, C., Ertmer, W., Krutzik, M., Lämmerzahl, C., Peters, A., Wicht, A., Windpassinger, P., Rasel, E.M.: Maius-b: A system for two-species atom interferometry in space. In: Proceedings of the 24th ESA Symposium on European Rocket and Balloon Programmes and Related Research (2019)

Roura, A., Zeller, W., Schleich, W.P.: Overcoming loss of contrast in atom interferometry due to gravity gradients. New. J. Phys. **16**(123012) (2014)

Schkolnik, V., Hellmig, O., Wenzlawski, A., Grosse, J., Kohfeldt, A., Döringshoff, K., Wicht, A., Windpassinger, P., Sengstock, K., Braxmaier, C., Krutzik, M., Peters, A.: A compact and robust diode laser system for atom interferometry on a sounding rocket. Appl. Phys. B **122**(8), 1–8 (2016). https://doi.org/10.1007/s00340-016-6490-0

Schlippert, D., Hartwig, J., Albers, H., Richardson, L., Schubert, C., Roura, A., Schleich, W., Ertmer, W., Rase, E.: Quantum test of the Universality of Free Fall. Phys. Rev. Lett. **112**(203002) (2014). https://doi.org/10.1103/PhysRevLett.112.203002

Shirley, J.H.: Modulation transfer processes in optical heterodyne saturation spectroscopy. Opt Lett **7**(11), 537–539 (1982)

Stamminger, A.: DLR's mobile rocket base - flight tickets for your microgravity experiments. Proc of the 64th International Astronautical Congress (2013)

Thalhammer, G., Barontini, G., Sarlo, L.D., Catani, J., Minardi, F., Inguscio, M.: Double species Bose-Einstein condensate with tunable interspecies interactions. Phys. Rev. Lett. **100**(210402) (2008)

Tsierkezos, N.G., Molinou, I.E.: Thermodynamic Properties of Water + Ethylene Glycol at 283.15, 293.15, 303.15, and 313.15 K. J. Chem. Eng. Data **43**(989-993) (1998). https://doi.org/10.1021/je9800914

Weps, B., Lüdtke, D., Franz, T., Maibaum, O., Wendrich, T., Müntinga, H., Gerndt, A.: A model-driven software architecture for ultracold gas experiments in space. In: Proceeding of the International Astronautical Congress, IAC. (2018)

Wicht, A., Bawamia, A., Krüger, M., Kürbis, C., Schiemangk, M., Smol, R., Peters, A., Tränkle, G.: Narrow linewidth diode laser modules for quantum optical sensor applications in the field and in space. In: Glebov AL, Leisher PO (eds) Components and Packaging for Laser Systems III, International Society for Optics and Photonics, SPIE, vol 10085. pp 103–118. (2017). https://doi.org/10.1117/12.2253655

Widmer, A.X., Franaszek, P.A.: A DC-balanced, partitioned-block, 8B/10B transmission code. IBM J Res Dev **27**(5), 440–451 (1983)

Wigley, P.B., Everitt, P.J., van den Hengel, A., Bastian, J.W., Sooriyabandara, M.A., McDonald, G.D., Hardman, K.S., Quinlivan, C.D., Manju, P., Kuhn, C.C.N., Petersen, I.R., Luiten, A.N., Hope, J.J., Robins, N.P., Hush, M.R.: Fast machine-learning online optimization of ultra-cold-atom experiments. Sci. Rep. **6**(25890) (2016)

Wildermuth, S., Krüger, P., Becker, C., Brajdic, M., Haupt, S., Kasper, A., Folman, R., Schmiedmayer, J.: Optimized magneto-optical trap for experiments with ultracold atoms near surfaces. Phys. Rev. A. **69**(30901 (R)) (2004)

Zhou, L., Long, S., Tang, B., Chen, X., Gao, F., Peng, W., Duan, W., Zhong, J., Xiong, Z., Wang, J., Zhang, Y., Zhan, M.: Test of equivalence principle at 10^{-8} level by a dual-species double-diffraction Raman atom interferometer. Phys. Rev. Lett. **115**(013004) (2015)